ELSEVIER

From ordered antiferromagnet to spin glass: A new phase $Mn_4Ir_{7-x}Mn_xGe_6$

T. Eriksson[a,*], P. Nordblad[b], Y. Andersson[a]

[a]Department Materials Chemistry, Uppsala University, Box 538, SE-751 21 Uppsala, Sweden
[b]Department Engineering Sciences, Uppsala University, Box 534, SE-751 21 Uppsala, Sweden

Abstract

A new ternary phase, $Mn_4Ir_{7-x}Mn_xGe_6$ ($0 \leqslant x \leqslant 1.3$), was studied by X-ray and neutron powder diffraction and SQUID magnetometry. The crystal structure is cubic, of the $U_4Re_7Si_6$ type, space group $Im\bar{3}m$, $Z = 2$, with the lattice parameter $a_{(x=0)} = 8.0326(2)$ Å at 295 K. Within the limited range of homogeneity small variations of the composition yield dramatic changes of the magnetic structure. For $x = 0$ long-range antiferromagnetic order is formed below the transition temperature 228 K, with large magnetic moments on Mn, 4.11(9) μ_B at 10 K, in a magnetic unit cell $a_M = b_M = \sqrt{2}a_C$, $c_M = 2a_C$. In contrast, for $x = 1.3$ spin glass behavior is observed below 90 K. The Mn atoms form an ideal cubic framework, on which geometric frustration of competing nearest and next nearest neighbor antiferromagnetic interactions is suggested to explain the composition sensitive magnetic properties. A TiNiSi-type phase, IrMnGe, is found in samples of 1:1:1 composition quenched from the melt.
© 2005 Elsevier Inc. All rights reserved.

1. Introduction

The ternary alloy phase diagrams of the Ir–Mn–Si and Ir–Mn–Ge systems have not been fully established. In recent articles we have reported the existence of the ordered phases Mn_3IrSi [1], Mn_3IrGe [2] and IrMnSi [3], all with interesting magnetic properties. Mn_3IrSi and Mn_3IrGe crystallize with the $AlAu_4$-type structure [4] and form similar commensurate non-collinear antiferromagnetic structures. The magnetic moments are found on a network of triangles of near neighbor Mn atoms, and as a result of geometric frustration the projections of the moments on the triangle planes form $120°$ angles [1]. IrMnSi crystallizes in the TiNiSi-type structure (ordered Co_2P) [5] and forms an incommensurate

cycloidal spiral magnetic structure below 460 K, with the propagation vector along the c-axis and spins rotating around an axis in the ab-plane [3]. Thus its magnetic structure is different from that of the isostructural and isoelectronic compound CoMnSi, which orders ferromagnetically above 390 K and at lower temperatures forms an incommensurate double screw spiral structure. In CoMnSi the spins rotate around the propagation vector, which is parallel to the c-axis [6,7].

In the course of studying the interplay between crystal structure and magnetic properties in ternary transition metal manganese silicides and germanides we have attempted to prepare the corresponding IrMnGe phase. However, IrMnGe turned out not no be stable in the equiatomic composition at 800 °C, as annealed samples were found to contain two phases: a majority phase of the $U_4Re_7Si_6$ type [8], corresponding to $Mn_4Ir_{7-x}Mn_xGe_6$ ($x = 1.3$), and Mn_3IrGe as minority

*Corresponding author. Tel.: +46 18 471 37 75;
fax: +46 18 51 35 48.

E-mail address: therese.eriksson@mkem.uu.se (T. Eriksson).

phase. Since the existence of the $Mn_4Ir_{7-x}Mn_xGe_6$ phase has not previously been reported, we have investigated the crystal structure and magnetic properties of $Mn_4Ir_{7-x}Mn_xGe_6$ ($0 \leqslant x \leqslant 1.3$) using X-ray and neutron powder diffraction and SQUID magnetometry.

2. Experimental

2.1. Sample preparation and phase analysis

Two master samples were prepared by the drop synthesis method [9]: one of composition $Mn_4Ir_7Ge_6$ (sample A) and one of composition IrMnGe (sample D). Starting materials were single crystal pieces of germanium (Highways International, purity 6 N), pressed pellets of iridium powder (Alfa Aesar, purity 99.95%) and pieces of manganese metal (Cerac, claimed purity 99.99%, purified from manganese oxides by sublimation). A high-frequency induction furnace, with 300 mbar argon atmosphere and the sample contained in an Al_2O_3 crucible, was used. Two samples of intermediate composition (sample B: 27.3 at% Mn; 38.2 at% Ir; 34.5 at% Ge, and sample C: 29.1 at% Mn; 36.8 at% Ir; 34.1 at% Ge) were prepared by melting mixtures of appropriate amounts of the two master samples under 300 mbar argon atmosphere in an arc furnace. After powderization, all samples were pressed into pellets and annealed in evacuated silica tubes for 3–4 days at 900 °C and 6–11 days at 800 °C. The samples used for neutron powder diffraction measurements (A, D) were stress relieved for 30 min at 800 °C.

Phase analysis and determination of unit cell dimensions were performed by powder X-ray diffraction using a Guinier–Hägg focusing camera ($CuK\alpha_1$ radiation) with Si added as internal standard ($a = 5.43088(4)$ Å at 295 K). X-ray powder diffraction intensities, used to estimate the respective phase fractions, were measured in transmission mode on a STOE & Cie GmbH STADI diffractometer ($CuK\alpha_1$ radiation), equipped with a position sensitive detector (PSD, $6°$ in 2θ).

2.2. Neutron powder diffraction

Neutron powder diffraction intensities were recorded for samples A and D, at the Swedish research reactor $R2$ in Studsvik, in the 2θ-range 4–139.92°, with steps of 0.08°. Measurements were performed at the temperatures 295, 150 and 10 K for sample D, and at 295, 190 and 10 K for sample A. The samples were contained in a vanadium cylinder and the neutron beam was monochromatised by two Cu (220) single crystals in parallel arrangement to give a wavelength $\lambda = 1.471$ Å. An absorption correction was applied using $\mu R = 1.47$ and 1.08 for sample A and D, respectively, as calculated from transmission measurements at $2\theta = 0°$.

2.3. Crystal and magnetic structure refinements

Crystal structure refinements were performed for neutron diffraction profiles, according to the Rietveld method, using the program FULLPROF [10]. The background was modeled by interpolation between fixed points. A pseudo-Voigt profile function with a refined ratio of Gaussian and Lorentzian contributions was used to describe the peak shape. The used scattering lengths were Ir: 10.6 fm; Mn: -3.73 fm; Ge: 8.185 fm [11]. The additional phases Mn_3IrGe (in sample D), and IrMn (in sample A) were included in the refinements and estimated to $\sim$15% and $\sim$10%, respectively, in mass of the samples.

For the 295 K neutron powder diffraction profiles, 17 and 18 parameters were varied, respectively, for samples A and D. Profile parameters: scale factor (1), zero point (1), profile shape parameter (1), half-width parameters (3), asymmetry parameters (2). Structural parameters: atomic coordinates (1), lattice parameters (1), isotropic temperature factors (4), partial occupancy factor (1). To avoid correlations, the occupancy parameter and the temperature factors were varied in alternate cycles of refinements. For samples A and D, respectively, 80 and 83 reflections were used in refinements for the main phase. For Mn_3IrGe and IrMn only scale factors (1) and lattice parameters (1 or 2, respectively) were varied (147 and 33 reflections, respectively).

For the 10 K neutron powder diffraction profiles for the $Mn_4Ir_7Ge_6$ composition, parameters describing the magnetic structure were also varied. A propagation vector ($\pm\mathbf{k} = \frac{1}{2}, \frac{1}{2}, \frac{1}{2}$) was used to describe the magnetic structure. Magnetic moments were localized on the Mn atoms (M_{Mn}: 1 parameter varied). An overall temperature factor was used. The nuclear and magnetic contributions to the diffraction intensities were treated as two separate phases, with the magnetic phase described in space group $P\bar{1}$, using the magnetic form factor curve of Mn^{3+}. Eighty reflections were used in refinements for the crystal structure, 38 reflections for the magnetic structure (only taken into account for $2\theta < 55°$), and 33 reflections for the IrMn phase.

2.4. Magnetization measurements

A Quantum Design MPMSXL SQUID magnetometer with a 5 T magnet and an ac-susceptibility option was used for magnetization and susceptibility measurements.

The magnetization of the $Mn_4Ir_{7-x}Mn_xGe_6$ samples A–D was measured in zero field cooled (zfc) and field cooled (fc) protocols from 10 to 300 K in an applied field of 250 Oe. Sample D was in addition investigated by low field ($H_{ac} = 4$ Oe) ac-susceptibility measurements at the frequencies: 0.17, 1.7, 17 and 170 Hz. The field dependence of the magnetization of samples A and D was recorded at some different temperatures.

3. Results

3.1. Phase analysis

After annealing at 800 °C the majority of the lines in the X-ray powder diffraction films could for all samples be indexed by a body centered cubic unit cell with a concentration dependent lattice parameter, see Table 1. The estimated Mn substitution (x) of $Mn_4Ir_{7-x}Mn_xGe_6$ in samples B and C, given in Table 1, was calculated assuming that the lattice parameter follows Vegard's law and that samples A and D correspond to $x = 0.0$ and 1.3, respectively, as obtained from crystal structure refinements (see below). Weak additional reflections were accounted for by the phases IrMn, IrGe or Mn_3IrGe. With the additional phases included in crystal structure refinements on X-ray powder diffraction intensities, the amounts were estimated to about 5 wt% IrMn in samples B, C; 15 wt% Mn_3IrGe in sample D; 10 wt% IrMn and 1 wt% IrGe in sample A.

If rapidly quenched from the melt, the majority phase in the sample of the equiatomic composition (sample D) was of the TiNiSi type [5], IrMnGe phase, and could be indexed on the primitive orthorhombic unit cell $a = 6.3171(6)$ Å; $b = 3.9741(4)$ Å; $c = 7.3120(8)$ Å. This phase completely disappears, already on annealing at 1050 °C, disintegrating into $Mn_4Ir_{7-x}Mn_xGe_6$ and Mn_3IrGe.

3.2. Crystal structure

The observed neutron powder diffraction intensities obtained at room temperature are well explained by a $U_4Re_7Si_6$-type structure [8], with the space group $Im\bar{3}m$. Mn occupies a 8c site, Ir a 2a and a 12d site, and Ge a 12e site, corresponding to two formula units of $Mn_4Ir_1Ir_6Ge_6$ (or, equivalently, $Mn_4Ir_7Ge_6$) per unit cell. For the composition IrMnGe (sample D) preferential substitution of Mn into the 12d site is observed. With the formula written as $Mn_4Ir_{7-x}Mn_xGe_6$ (or, strictly, $Mn_4Ir_1Ir_{6-x}Mn_xGe_6$), the occupancy obtained from crystal structure refinements corresponds to $x = 1.33(3)$. If the ratio of Ir/Mn occupancy of the 12d site is varied during refinements also for the $Mn_4Ir_7Ge_6$ composition (sample A), a small deviation from pure Ir occupancy is obtained (six times the estimated standard deviation, corresponding to $x < 0.2$), but with only minor improvements of the agreement factors. No significant partial Mn occupancy of the other crystallographic sites was found for either sample A or D. The structural parameters and agreement factors obtained in crystal structure refinements for samples A and D at room temperature are listed in Table 2, and the observed and calculated profiles are shown in Figs. 1 and 2, respectively. For both samples the crystal structure remains unchanged down to 10 K.

The $Mn_4Ir_7Ge_6$ crystal structure can be viewed as composed of eight Cu_3Au-related sub-units with Mn atoms at the corners and with Ge and Ir/Mn atoms occupying the face centre positions in an ordered manner. Every fourth Cu_3Au sub-unit is filled with an Ir atom, octahedrally coordinated by six Ge atoms, and three out of four sub-units contain empty distorted octahedra of four Ir/Mn and two Ge atoms. The distortion arises as the Ge atoms of the Ir-filled octahedra are displaced outwards from the octahedron center and thus out of the face center of the Cu_3Au sub-unit. The crystal structure is illustrated in Fig. 3, which

Table 1
Lattice parameter and estimated Mn substitution (x) in $Mn4Ir_{7-x}Mn_xGe_6$ for samples A–D at 295 K

Sample	a (Å)	x
A	8.0326(2)	0.0
B	8.0354(2)	0.5
C	8.0394(2)	1.1
D	8.0404(2)	1.3

Table 2
Final crystal structure parameters and agreement factors for samples A and D at 295 K

Atom	Wyckoff site	Coordinates	Sample A B (Å²)	Sample D B (Å²)
Mn	8c	$\frac{1}{4},\frac{1}{4},\frac{1}{4}$	0.8(1)	0.6(1)
Ir1	2a	0, 0, 0	0.5(1)	0.7(1)
Ir/Mn2	12d	$\frac{1}{4}, 0, \frac{1}{2}$	1.12(6)	0.69(7)
Ge	12e	$x, 0, 0$	0.85(7)	0.75(6)
Sample A	$x_{Ge} = 0.3075(4)$		Occupancy Ir/Mn2 = 100% Ir	
	$R_p = 4.02\%$; $R_{wp} = 5.08\%$; $R_{exp} = 4.40\%$; $\chi^2 = 1.34$; $R_{Bragg} = 7.29\%$			
Sample D	$x_{Ge} = 0.3060(3)$		Occ. Ir/Mn2 = 77.8(5)% Ir, 22.2(5)% Mn	
	$R_p = 3.84\%$; $R_{wp} = 4.82\%$; $R_{exp} = 4.08\%$; $\chi^2 = 1.39$; $R_{Bragg} = 5.71\%$			

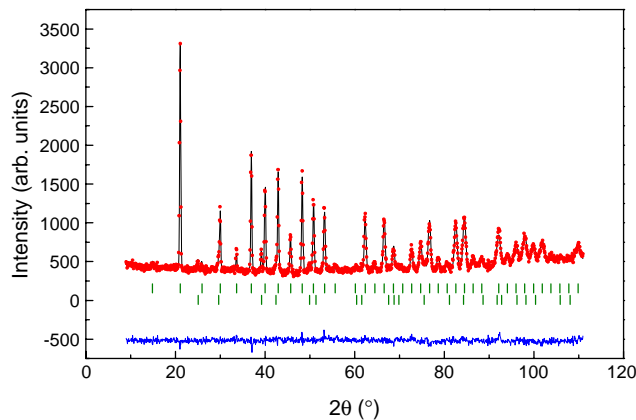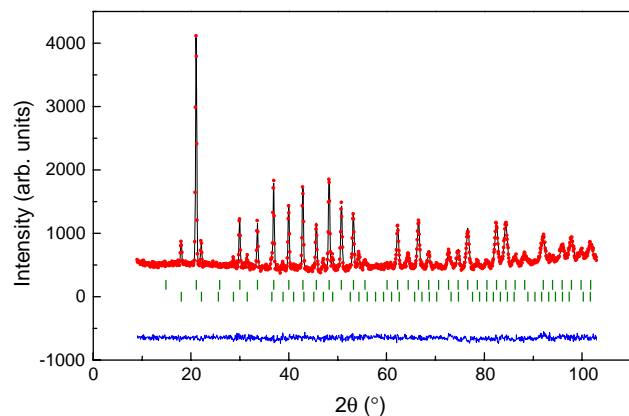Estimated standard deviations within parentheses. Space group $Im\bar{3}m$ (No. 229).

Fig. 1. Observed (points), calculated (solid line), and difference (observed–calculated; bottom solid line) neutron powder diffraction profiles at 295 K for sample A ($Mn_4Ir_7Ge_6$ composition). Upper tick marks indicate the positions of Bragg reflections for the $Mn_4Ir_7Ge_6$ phase, and lower tick marks for the IrMn phase.

Fig. 2. Observed (points), calculated (solid line), and difference (observed–calculated; bottom solid line) neutron powder diffraction profiles at 295 K for sample D (IrMnGe composition). Upper tick marks indicate the positions of Bragg reflections for the $Mn_4Ir_7Ge_6$ phase, and lower tick marks for the Mn_3IrGe phase.

Fig. 3. The $Mn_4Ir_7Ge_6$ crystal structure. The box (black line) of one unit cell is drawn, with the cell contents of the range $-0.25 < x < 1.25$; $-0.25 < y < 1.25$; $0.25 < z < 0.75$ inserted. Links between Mn atoms are added to illustrate the Cu_3Au-related sub-units (Mn atoms at the corners).

Table 3
Interatomic distances (< 3.5 Å) in $Mn_4Ir_7Ge_6$ (sample A) at 295 K

Atoms	Distance (Å)	Atoms	Distance (Å)
Mn–6 Ir/Mn2	2.840(1)	Ir1–6 Ge	2.470(3)
Mn–6 Ge	2.877(1)	Ir1–8 Mn	3.478(1)
Mn–2 Ir1	3.478(1)	Ge–Ir1	2.470(3)
Ir/Mn2–4 Ge	2.534(2)	Ge–4 Ir/Mn2	2.534(2)
Ir/Mn2–4 Ir/Mn2	2.840(1)	Ge–4 Mn	2.877(1)
Ir/Mn2–4 Mn	2.840(1)	Ge–Ge	3.092(6)
		Ge–4 Ge	3.493(4)

Fig. 4. The Mn coordination sphere of six Ir/Mn2 atoms and six Ge atoms, which links the Mn atoms via the face center positions, as illustrated by dashed bonds in (a) and solid links on one face of two Cu_3Au sub-units in (b).

shows a slab one Cu_3Au sub-unit thick. The centering translation by $\frac{1}{2}, \frac{1}{2}, \frac{1}{2}$ repeats this slab in the next layer of Cu_3Au units.

Interatomic distances shorter than 3.5 Å were calculated and are listed in Table 3. The Mn atoms are 12 coordinated by six Ir/Mn atoms in one plane, three Ge atoms above and three Ge atoms below, corresponding to the face center positions of the Cu_3Au sub-units, as illustrated by dashed bonds in Fig. 4(a) and solid links on one side of two Cu_3Au sub-units in Fig. 4(b). The Ir atoms are octahedrally coordinated by Ge, as described above. The Ir/Mn atoms are coordinated by four nearest neighbor Ge atoms forming a highly distorted tetrahedron, with four Ir/Mn atoms forming a second, larger, distorted tetrahedron and four Mn atoms forming a square planar coordination, see Fig. 5(a). Ge is coordinated by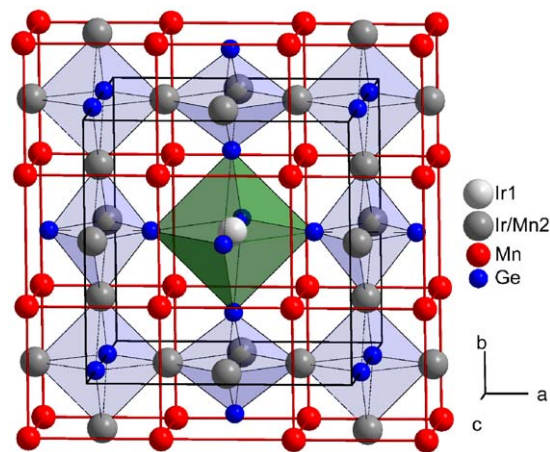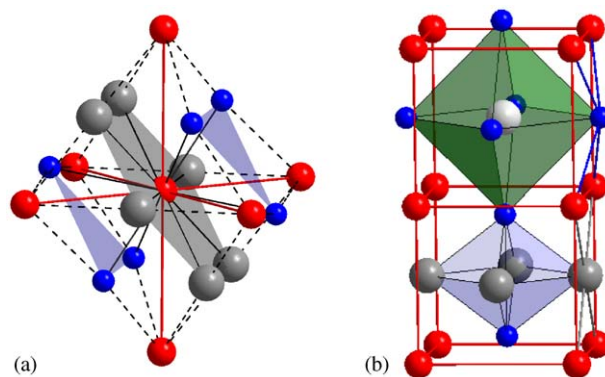 four Ir/Mn atoms and one Ir atom forming a distorted square pyramid, which is inscribed in a larger distorted square pyramid of four Mn atoms and one Ge atom, see Fig. 5(b).
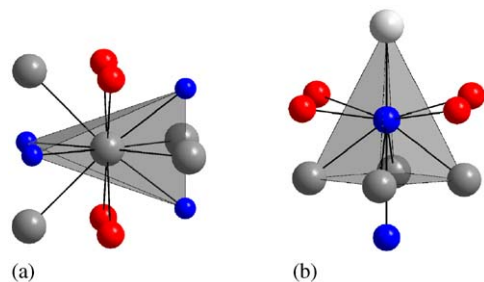
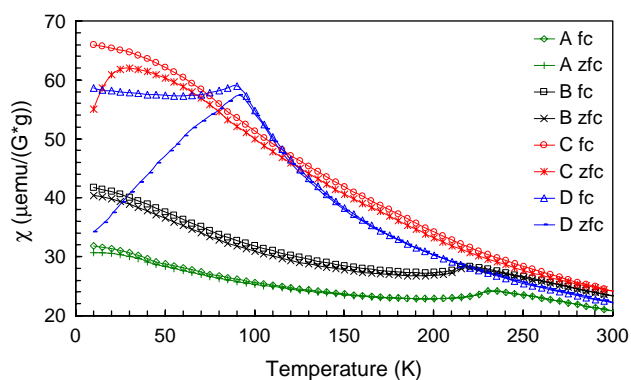Fig. 5. (a) The Ir/Mn2 coordination sphere and (b) the Ge coordination sphere.

Fig. 7. Frequency dependence of the in-phase component of the ac-susceptibility (χ') vs. temperature for sample D ($Mn_4Ir_{7-x}Mn_xGe_6$, $x = 1.3$).

Fig. 6. Temperature dependence of the field cooled (fc) and zero-field cooled (zfc) magnetic susceptibility (χ) of $Mn_4Ir_{7-x}Mn_xGe_6$ for samples with $x = 0$ (A); $x = 0.5$ (B); $x = 1.1$ (C); and $x = 1.3$ (D).

3.3. Magnetization measurements

Fig. 6 shows the zfc and fc susceptibility ($\chi = M/H$) of the four different samples in the temperature range 10–300 K. Samples A ($x = 0$) and B ($x = 0.5$) both show a weakly varying susceptibility with temperature, however with a clear anomaly at, respectively, about 230 and 210 K indicating an antiferromagnetic phase transition. The very temperature of the transition, determined from plots of $d(\chi T)/dT$ vs. T, is 228 and 212 K, respectively. Magnetization vs. field curves on sample A yield linear behavior both above and below the transition temperature. The magnitude of the susceptibility of samples A and B varies within the range $20–40 \times 10^{-6}$ emu/g Oe in the measured temperature interval. The susceptibility does not show Curie–Weiss behavior above the transition temperature for these two samples.

Sample C ($x = 1.1$) shows, as is seen in Fig. 6, a rather featureless continuous increase of the fc susceptibility with decreasing temperature and always a somewhat higher susceptibility value than samples A and B. There is no indication of a phase transition in the fc curve, however, there appears a quite strong irreversibility between the zfc and fc susceptibility curves at temperatures below 50 K.
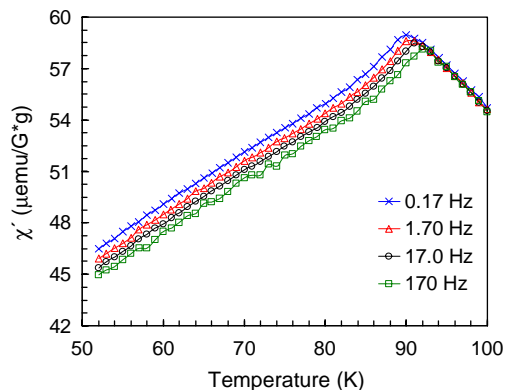
Sample D ($x = 1.3$) shows a rather sharp maximum in the zfc susceptibility curve at about 90 K, and onset of a strong irreversibility between the zfc and fc curves at about the same temperature. The sharp maximum in the zfc and the flattening out of the fc susceptibility at temperatures below this maximum have similarities with spin glass behavior. To further elaborate on this possibility, Fig. 7 shows the in-phase component of the ac-susceptibility (χ') vs. temperature at four different frequencies between 0.17 and 170 Hz. The maximum in χ' shifts to higher temperatures with increasing frequency and the maximum in the in-phase component is accompanied by the onset of a finite out-of-phase component of the susceptibility with decreasing temperature. It is also worth to mention that a magnetization vs. field (-10 to 10 kOe) curve measured at 80 K on this sample shows a weak non-linear behavior (S-shape) and some hysteresis. All these features are indicative of the appearance of a low temperature spin glass phase.

3.4. Magnetic structure

The neutron powder diffraction pattern recorded at 10 K for the $Mn_4Ir_7Ge_6$ composition (sample A) shows extra reflections due to magnetic order in the sample (see Fig. 8), which cannot be indexed using the unit cell of the crystal structure. These super-structure reflections arise from an antiferromagnetic ordering of the magnetic moments, and can be indexed by a magnetic unit cell where a_M and b_M correspond to the face diagonals of the crystallographic unit cell and c_M is twice the crystallographic unit cell axis ($a_M = b_M = \sqrt{2}a_C$, $c_M = 2a_C$), see Fig. 9, which gives a magnetic unit cell with four times the volume of the crystallographic unit cell. As is also shown in Fig. 9, a larger magnetic unit cell with a doubling of all the crystallographic axes (giving eight times the volume of the crystallographic unit cell), can also be chosen. Thus a propagation vector

$\mathbf{k} = (\frac{1}{2}, \frac{1}{2}, \frac{1}{2})$ was used in magnetic structure refinements, rendering a magnetic moment of $4.11(9)\,\mu_B$ on the Mn atoms, with no significant moments on the Ir or Ge atoms. The parameters obtained in the last cycles of refinements are listed in Table 4. Unfortunately, the overlapping reflections of the powder pattern make it impossible to determine the directions of the magnetic moments relative to the crystallographic axes. We are also unable to distinguish between different possible arrangements of the relative magnetic moment directions on the Mn atoms.

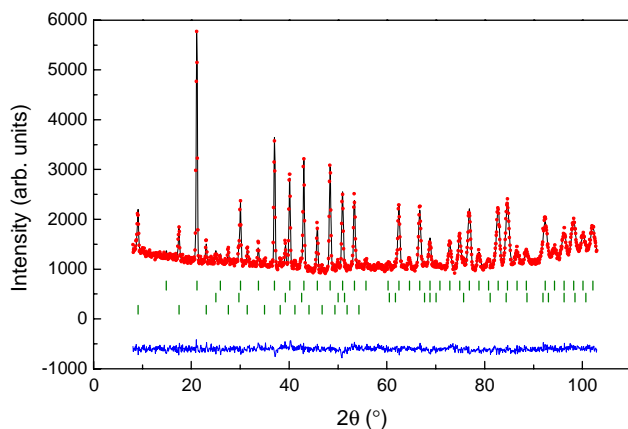As can be seen in the crystal structure drawing in Fig. 3 the Mn atoms form an ideal simple cubic

Fig. 8. Observed (points), calculated (solid line), and difference (observed−calculated; bottom solid line) neutron powder diffraction profiles at 10 K for sample A ($Mn_4Ir_7Ge_6$ composition). Upper tick marks indicate the positions of Bragg reflections for the $Mn_4Ir_7Ge_6$ crystal structure, middle line tick marks for the IrMn phase, and lower tick marks for the $Mn_4Ir_7Ge_6$ magnetic structure.
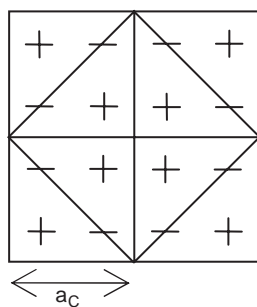

Fig. 9. The relation between the crystallographic (a_C) and magnetic (a_M, c_M) unit cell is $a_M = b_M = \sqrt{2}a_C$, $c_M = 2a_C$. The magnetic moment $(+ - - +)$ repeat sequence is shown.

framework, of which the cube axes are exactly half the length of the unit cell axes. Thus in order for the observed magnetic super-structure reflections to arise, the magnetic moments of the second nearest Mn atoms along the cube axes must align antiferromagnetically. One way of achieving this is a $(+ - - +)$ sequence, which can be formed by collinear magnetic moments, illustrated in Fig. 9 for the base plane, and in three dimensions using open and filled circles for opposite magnetic moment directions in Fig. 10(a). Another possible model is to have two magnetic sub-lattices with orthogonal moment directions, as illustrated in Fig. 10(b). To evaluate different possible magnetic ordering schemes, a single crystal neutron diffraction study is needed.

For $Mn_4Ir_{7-x}Mn_xGe_6$, $x = 1.3$ (sample D), the neutron powder diffraction pattern recorded at 10 K is very similar to the pattern recorded at 295 K. No extra peaks indicative of magnetic long-range order can be seen, and there is also no significant increase of diffuse scattering, which would indicate short-range magnetic order. This is in agreement with the observed spin glass like behavior in the corresponding magnetization curves.

4. Discussion and conclusions

We have identified a new phase, $Mn_4Ir_{7-x}Mn_xGe_6$, which crystallizes with the $U_4Re_7Si_6$-type structure [8] and shows a solid solubility range of about 8 at% Mn. An orthorhombic IrMnGe phase, crystallizing in the TiNiSi-type structure [5], is only obtained in samples of the equiatomic composition rapidly cooled from the melt.

Numerous rare earth transition metal germanides and a few silicides with the $U_4Re_7Si_6$-type structure are reported, see, e.g., [8,12–17]. For these, examples of all types of magnetic properties can be found in reports of magnetization measurements, e.g., ferromagnetism in $U_4Ru_7Ge_6$ [15], antiferromagnetism in $U_4Tc_7Si_6$ [17] and $Tb_4FeGa_{12-x}Ge_x$ [18], and paramagnetism down to low temperatures in $U_4Os_7Ge_6$ [15] and $Yb_4(Ir/Rh)_7Ge_6$ [16]. To our knowledge there are no previous reports of magnetic structure investigations by neutron diffraction for $U_4Re_7Si_6$-type compounds.

Table 4
Final structural parameters, magnetic moment and agreement factors for $Mn_4Ir_7Ge_6$ (sample A) at 10 K

a (Å)	x_{Ge}	$B_{overall}$ (Å^2)	M_{Mn} (μ_B)
8.0248(4)	0.3079(3)	0.16(3)	4.11(9)

$R_p = 2.71\%$; $R_{wp} = 3.37\%$; $R_{exp} = 2.76\%$; $\chi^2 = 1.50$; $R_{Bragg} = 5.66\%$; $R_{mag} = 9.97\%$
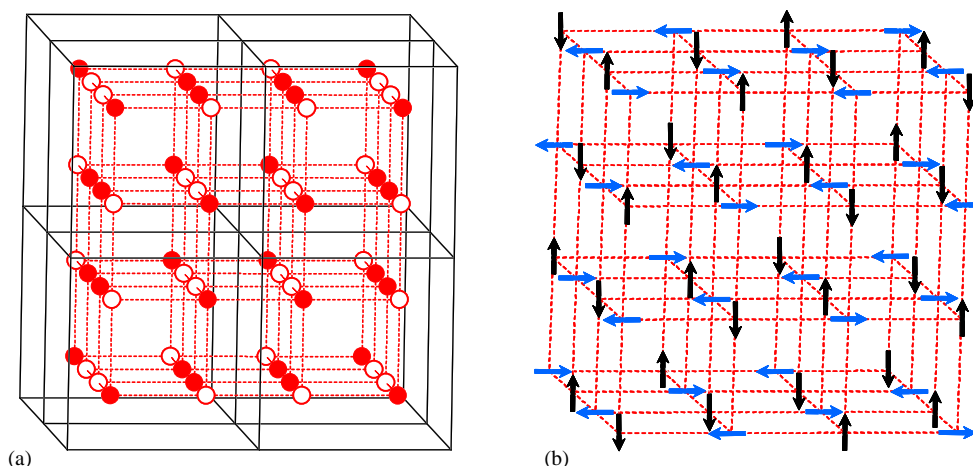
Estimated standard deviations within parentheses.

Fig. 10. Possible magnetic ordering schemes. The ideal cubic framework of Mn atoms within the magnetic unit cell ($a_M = 2a_C$) indicated by dashed bonds. (a) The crystallographic unit cell edges shown as solid lines. Open and closed circles represent opposite spin directions. (b) Orthogonal magnetic sublattices. Same unit cell content as in (a) but the unit cell edges have been omitted.

We find antiferromagnetic order below $228\,K$ for $Mn_4Ir_{7-x}Mn_xGe_6$ with $x = 0$, with magnetic moments of $4.11(9)\,\mu_B$ at $10\,K$ on the Mn atoms. When Ir is substituted by Mn (x increases), a decrease of the magnetic transition temperature as well as loss of long-range magnetic order occur, and spin-glass properties are shown for the sample with the largest Mn concentration ($x = 1.3$).

The crystallographic unit cell holds eight Mn atoms at the corners of a perfect cube, with fairly large Mn–Mn separation ($4.012\,\text{Å}$ at $10\,K$). If antiferromagnetic interactions between nearest neighbor Mn atoms were dominating, an antiferromagnetic ordering of the magnetic moments could be achieved within the crystallographic unit cell. In contrast, indexing of the magnetic super-structure reflections observed in the neutron diffraction patterns require a larger magnetic unit cell ($a_M = b_M = \sqrt{2}a_C$, $c_M = 2a_C$), suggesting that antiferromagnetic interactions between next nearest Mn atoms along the face diagonals of the Mn cubes must be considered. Nearest and next nearest neighbor antiferromagnetic interactions of comparable strength would in this geometry give rise to magnetic frustration, since both cannot be satisfied on the corners of the cubic network, as discussed by, e.g., Saes et al. for the square planar lattice [19].

When Ir is substituted for Mn (x increases), the additional Mn atoms occupy a fraction of the face centre positions of the Mn cubes. The resulting random distribution of short local Mn–Mn distances ($2.840\,\text{Å}$ at $10\,K$), with expected strong magnetic interactions, can explain the observed spin glass properties in the Mn rich compound.

The transition from long-range ordered antiferromagnetic structure to spin glass behavior, caused by adding a few atomic percent manganese, is an interesting property of the $Mn_4Ir_{7-x}Mn_xGe_6$ phase. Possibly the sensitivity to the composition is an effect of geometric frustration of competing antiferromagnetic interactions on the cubic framework of Mn atoms.

References

[1] T. Eriksson, R. Lizárraga, S. Felton, L. Bergqvist, Y. Andersson, P. Nordblad, O. Eriksson, Phys. Rev. B 69 (2004) 054422.
[2] T. Eriksson, L. Bergqvist, P. Nordblad, O. Eriksson, Y. Andersson, J. Solid State Chem. 177 (2004) 4058–4066.
[3] T. Eriksson, L. Bergqvist, T. Burkert, S. Felton, R. Tellgren, P. Nordblad, O. Eriksson, Y. Andersson, Phys. Rev. B, accepted.
[4] O.E. Ullner, A. Kemi, Mineral. Geol. 14A (1940) 1–20.
[5] C.B. Shoemaker, D.P. Shoemaker, Acta Crystallogr. 18 (1965) 900–905.
[6] H. Bińczycka, A. Szytuła, J. Todorović, T. Zaleski, A. Zięba, Phys. Status Solidi A 35 (1976) K69–K72.
[7] S. Nizioł, H. Bińczycka, A. Szytuła, J. Todorović, R. Fruchart, J.P. Senateur, D. Fruchart, Phys. Status Solidi A 45 (1978) 591–597.
[8] L.G. Aksel'rud, Y.P. Yarmolyuk, E.I. Gladyshevskii, Dopov. Akad. Nauk Ukr. RSR Ser. A 4 (1978) 359–362.
[9] S. Rundqvist, Chem. Scr. 28 (1988) 15–20.
[10] J. Rodríguez-Carvajal, FULLPROF Computer Program, version 2.80, LLB, Saclay, 2004.

[11] V.F. Sears, Neutron News 3 (1992) 26–37.

[12] N. Engel, B. Chabot, E. Parthé, J. Less-Common Met. 96 (1984) 291–296.

[13] M. Francois, G. Venturini, J.F. Marêché, B. Malaman, B. Roques, J. Less-Common Met. 113 (1985) 231–237.

[14] B. Heying, K. Katoh, Y. Niide, A. Ochiai, R. Pöttgen, Z. Anorg. Allg. Chem. 630 (2004) 1423–1426.

[15] B. Lloret, B. Buffat, B. Chevalier, J. Etourneau, J. Magn. Magn. Mater. 67 (1987) 232–238.

[16] K. Katoh, H. Abe, D. Negishi, G. Terui, Y. Niide, A. Ochiai, J. Magn. Magn. Mater. 279 (2004) 118–124.

[17] F. Wastin, J. Rebizant, J.P. Sanchez, A. Blaise, J. Goffart, J.C. Spirlet, C.T. Walker, J. Fuger, J. Alloys Compds. 210 (1994) 83–89.

[18] M.A. Zhuravleva, X. Wang, A.J. Schultz, T. Bakas, M.G. Kanatzidis, Inorg. Chem. 41 (2002) 6056–6061.

[19] M. Saes, N.P. Raju, J.E. Greedan, J. Solid State Chem. 140 (1998) 7–13.